ChemCatChem

Research Article
doi.org/10.1002/cctc.202500738

Chemistry Europe
European Chemical Societies Publishing

www.chemcatchem.org

Efficient Anodized WO_3 Photoanode for Photoelectrocatalytic Applications: Hydrogen Production and Reduction of CO_2

Alberto Pérez-Calvo,[a] Ginebra Sánchez-García,[a] Gemma Roselló-Márquez,[a] Encarna Blasco-Tamarit,[b] Ramón M. Fernández-Domene,[a] Rita Sánchez-Tovar,*[a] and Benjamín Solsona*[a]

In this work, a nanostructured WO_3 photoanode has been used for photoelectrochemical H_2 production and CO_2 reduction. In particular, we provide a novel method to synthesize tungsten oxide catalysts by anodization of tungsten using an ionic liquid, [EMIN][BF_4], as electrolyte in hydrodynamic conditions. We found that the use of appropriate hydrodynamic conditions (200–400 rpm) provides larger and more homogenous nanostructures with higher surface area. All this leads to better morphological and electrochemical properties. An excessive rotation during the synthesis (600 rpm) breaks the uniformity of the morphology of the nanostructures, thus hindering the photoelectrochemical performance. This way, the use of an optimized WO_3 photoanode has shown excellent potential for photoelectrocatalytic water splitting. Moreover, these nanostructures also present good performance in the photoelectrocatalytic CO_2 reduction, leading to the main formation of acetic acid, formic acid, and methanol. In fact, after only 6 h in continuous mode, a remarkable formic acid concentration of 190 µmol/L at 6 h has been obtained. Moreover, we have illustrated the great importance of the anode during the PEC reaction, significantly influencing the concentration of the obtained products owing to the electrons and protons transferred from the oxygen evolution reaction (OER).

1. Introduction

In the last century, the growth of the human population and the increase in the use of fossil fuels have produced an increase in the emission of greenhouse gases, this one being the main cause of global warming.[1] Carbon dioxide (CO_2) is the major greenhouse gas, well above the following ones, methane (CH_4) and nitrous oxide (N_2O).[1,2] Consequently, due to the need for reducing anthropogenic CO_2 emissions into the environment, various techniques have been studied in order to promote the decarbonization economy.[3,4] Inside the line of carbon capture and utilization (CCU), a very interesting approach is the photoelectrocatalytic transformation that allows producing high added value products from CO_2 such as methane, methanol, formic acid, acetic acid, and so on, depending on the electrolyte and the catalysts used.[4–8] This method is based on the reduction of carbon dioxide in the cathode by applying a small external potential and illuminating the semiconductor (cathode or anode), promoting pairs of electrons (e^-)/holes (h^+), which are responsible for carrying out redox reactions producing the desired products (Figure 1A).[9–11] In addition, the possibility of combining electro- and photocatalytic approaches allows increasing the formation of charge carriers (e^-/h^+) and reducing their recombination, improving the efficiency of the process and managing better yields.[7,12,13]

Unfortunately, the CO_2 molecule is very stable due to its strong bonds. Therefore, it takes a lot of energy to break those bonds and transform CO_2.[3] Moreover, the solubility of CO_2 in aqueous solutions is low, and its absorption and activity are lower than water, leading to low selectivities to the desired carbonaceous products.[14] To improve this, an important factor to be controlled in the CO_2 reduction process is the nature of the catalyst. Thus, the type of the nanostructure and the morphology determine the catalytic performance.[15,16] Therefore, it is important to use a method that allows modifying many parameters during the synthesis, such as electrochemical anodization. This technique works at atmospheric pressure and suitable temperature and can produce materials with different properties by adjusting a variety of operation factors, such as the temperature, electrolyte composition, and the applied cell potential. For this reason, anodization is a very useful process with little effect on the environment.[17,18] Moreover, this technique permits the nanostructure to be obtained directly adhered to the

[a] A. Pérez-Calvo, G. Sánchez-García, G. Roselló-Márquez, R. M. Fernández-Domene, R. Sánchez-Tovar, B. Solsona
Chemical Engineering Department (ETSE), Universitat de València, Av. Universitat s/n, Burjassot, Valencia 46100, Spain
E-mail: rita.sanchez@uv.es
benjamin.solsona@uv.es

[b] E. Blasco-Tamarit
Instituto Universitario de Seguridad Industrial, Radiofísica y Medioambiental (ISIRYM), Universitat Politècnica de València, Camino de Vera s/n, Valencia 46022, Spain

Supporting information for this article is available on the WWW under https://doi.org/10.1002/cctc.202500738

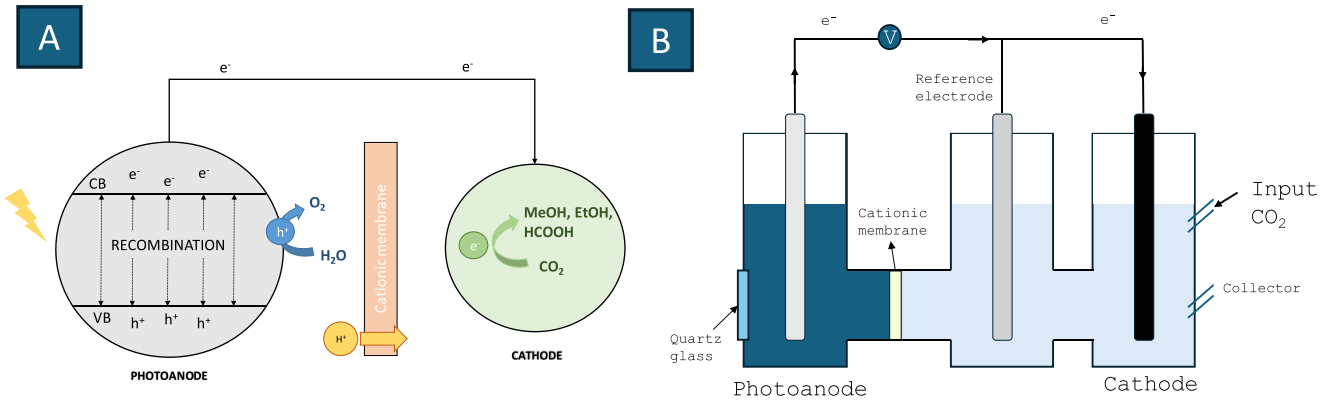

Figure 1. (A) Schematic CO_2 photoelectroreduction irradiating the anode and (B) H-type cell used for the PEC CO_2 reduction.

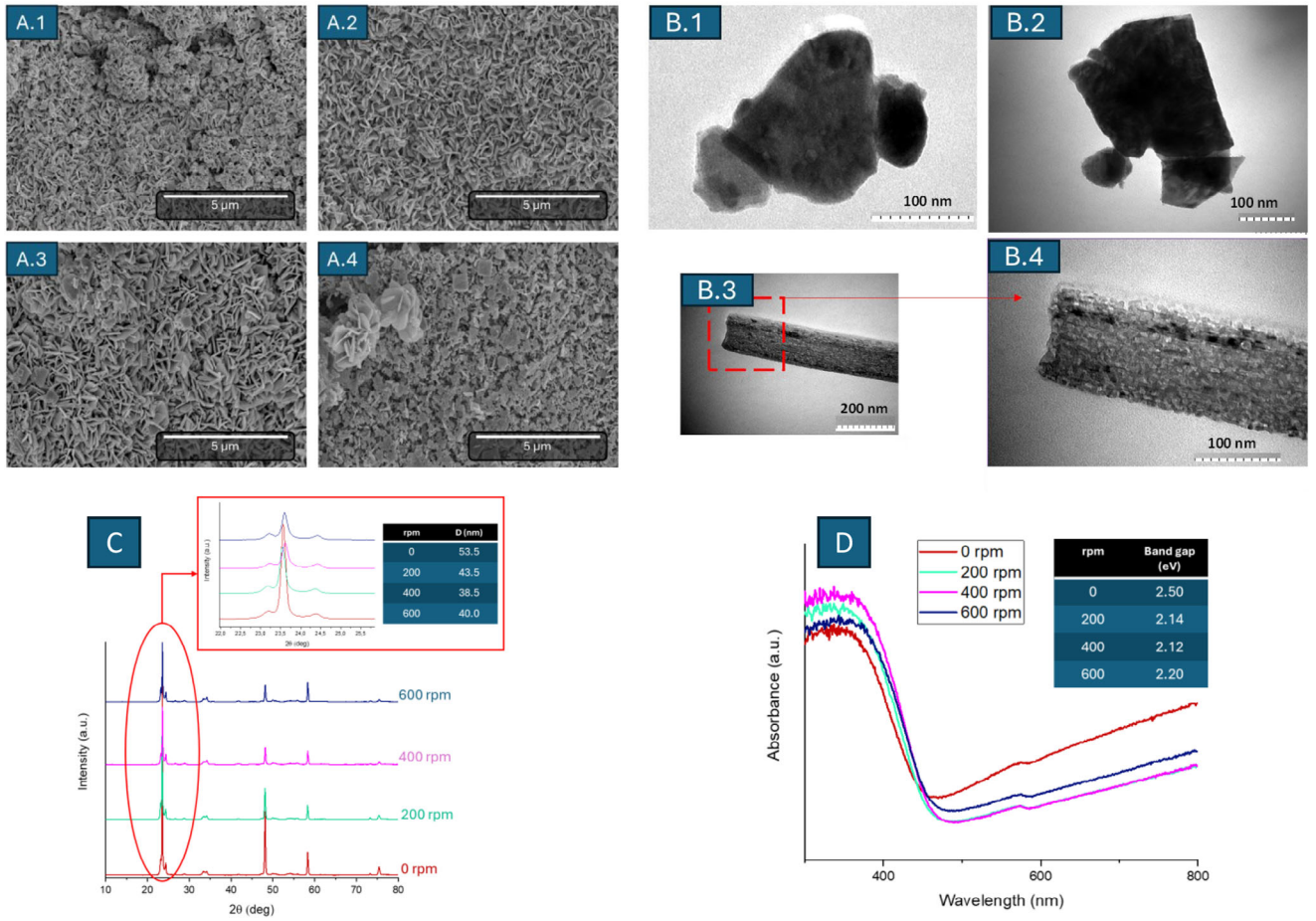

Figure 2. (A) FESEM images of the WO_3 nanostructures in the presence of agitation at different rotation speed. 1) 0 rpm, 2) 200 rpm, 3) 400 rpm, and 4) 600 rpm. (B) Transmission electron microscopy (TEM) images of the WO_3 samples synthesized with ionic liquid during the anodization process: 1) static conditions, 2) hydrodynamic conditions (600 rpm), 3) and 4) hydrodynamic conditions (400 rpm), 4) hydrodynamic conditions (400 rpm) with different magnification. (C) XRD patterns of WO_3 nanostructures synthesized at 0, 200, 400, and 600 rpm. (D) DR-UV–vis spectra of WO_3 samples anodized at different hydrodynamic conditions (0, 200, 400, and 600 rpm).

metallic substrate, without any intermediate step. This improves conductivity and decreases e^-/h^+ pair recombination.[18]

To enhance the process performance, significant efforts must be made to lower the reaction overpotential and to improve the transformation of CO_2.[19] Different metal semiconductors have been used to transform CO_2 into new valuable products such as TiO_2,[19] $BiVO_4$,[20] WO_3,[21] Fe_2O_3,[22] and so on, as the anode material and CuO_x,[23] InP,[24] GaN[25] as cathodes. Copper-based materials exhibit unique properties in converting CO_2 into multi-carbon products such as ethanol and acetic acid.[26] Extensive research has been devoted in order to improve the design of photoelectrocatalysts and enhance CO_2 conversion efficiency,

particularly through the development of nanostructured anodes for the photoelectroreduction of CO_2 using solar energy. In the case of the anode, although it does not interfere with the direct reduction of carbon dioxide, several studies show its importance during the reaction of CO_2.[27,28] Hence, it plays a very important role, providing protons and electrons from the water oxidation to facilitate the reduction of CO_2 and increasing the extra negative potential to the cathode, converting light into electricity.

One promising alternative to fossil fuels as a strategy for reducing CO_2 emissions is hydrogen, which presents a wide range of beneficial applications. For instance, hydrogen can be used in fuel cell technologies for electricity generation and also serves as a fuel in internal combustion engines or turbines.[29] Photoelectrochemical (PEC) hydrogen production is a highly efficient and environmentally friendly approach that uses solar energy (and a small potential bias) to generate hydrogen. This method addresses a major challenge in the transition to renewable energy. In PEC systems, light exposure drives electrochemical reactions, with photons playing a central role. Among the different hydrogen production processes, PEC stands out for its ability to generate high-purity hydrogen from water without carbon emissions, using low-cost materials under very mild ambient conditions.[30] However, as hydrogen gains attraction as a clean energy alternative, there is an increasing demand for effective and economical methods of its storage and transportation. In this context, materials like formic acid and acetic acid have recently attracted interest as hydrogen carriers. These compounds are especially compelling because they can be synthesized from CO_2, offering the potential for a closed-loop carbon system.[29]

Tungsten trioxide (WO_3) is an n-type semiconductor that can act as a photoanode with a suitable banggap of 2.5–2.8 eV (high visible-light activity), which presents good stability in acidic solutions and large hole diffusion (150 nm).[31] For these reasons, it has been used in many electronic and environmental applications.[32] However, its practical performance remains significantly below the theoretical potential, since WO_3 photoanodes face several challenges, including a short excited-state lifetime, unfavorable band-edge alignment, sluggish oxygen evolution reaction (OER) kinetics, and susceptibility to photocorrosion.[33] In order to improve their photoelectrocatalytic performance, some methods, such as solvothermal,[34] combustion,[35] hydrothermal,[36] chemical vapor deposition,[37] electrodeposition,[38] and sol–gel,[39] have been used to manage different morphologies (nanoplates, nanoflakes, nanowires, etc.)[40] and to get nanostructures with high surface area, low bandgap, and short diffusion lengths. Most of these methods result in powders with a variety of morphologies (nanoplates, nanosheets, etc.), but on many occasions, they use corrosive chemicals, nonreusable solutions, or a lot of energy during fabrication.[41] Thus, the use of ionic liquids (ILs) as electrolytes in the anodization could be a solution thanks to their good environmental characteristics and their nonvolatility, very good recyclability, and non-flammability.[42,43] It is well known that these types of liquids are effective in controlling the morphology, size, and structure of the nanomaterials, improving their performance.[44,45] Besides, it has been proven that their action during synthesis is better than that of deep eutectic solvents (DES) for some nanostructured semiconductors, such as TiO_2.[45] Thus, the ionic liquid [EMIM][BF_4] can interact between precipitated particles of tungsten and fluoride anions generated in situ, forming stronger bonds and nanostructures with better photoelectrocatalytic behavior.[41]

Recently, tungsten trioxide (WO_3) has gained special attention as a promising photoanode material for several applications. However, despite the progress and the interesting opportunities presented by the photoelectrochemical transformation of carbon dioxide or the photoelectrochemical water splitting, adequate results have not been obtained yet, and the proposed methods have low scalability. Therefore, in this study, we synthesized WO_3 nanostructures by anodizing tungsten sheets, with the aim of using them as photoanodes under solar illumination in two applications of paramount importance: PEC-water splitting and the continuous photoelectroreduction of CO_2, to enhance both the selectivity and conversion efficiency toward formic acid and related compounds.

2. Results and Discussion

2.1. WO_3 Nanostructures (photoanodes)

Tungsten anodization follows the typical dissolution–precipitation mechanism.[46,47] During this process, a compact layer of WO_3 is formed on the substrate due to the applied potential between the anode and cathode (Equation 1). Then, the previously generated oxide layer dissolves as a result of the presence of cations (H^+) in the methanesulfonic acid solution (Equation 2). Since ionic liquids have a low dielectric constant, they decrease the ionic mobility in the solution during this second step. According to this fact, WO_2^{2+} formed in the solution are easily precipitated on the anodized tungsten. This mechanism is increased due to the BF^- anions that tend to form soluble complexes with tungsten and further favor the dissolution of the oxide layer (Equation 3).[45] The nanostructured layer is created when the soluble tungsten species that have been dissolved in the solution finally achieve saturation and precipitate on the substrate surface as a hydrated tungsten oxide (Equation 4).

Field emission scanning electron microscope (FESEM) images of the anodized samples at different speeds are shown in Figure 2A. There it can be observed a nanostructured surface with a morphology similar to nanoplates.

Table 1 shows the length (L) and thickness (th) of the tungsten nanostructures anodized at different rotation speeds. According to Table 1, rotating the electrode during anodization increases the length of the nanostructures. Additionally, for higher rotation speeds variation in the size and uniformity of the anodized surfaces become more apparent. That is, an increase in the length of the nanoplates from 0.40 μm at 0 rpm until a maximum of 0.71 μm at 400 rpm. However, when rotation speed

Table 1. Length, width, and thickness measures for the WO_3 nanostructures anodized at different revolutions.

WO_3 Sample (rpm)	Length (μm)	Width (μm)	Thickness (μm)
0	0.40 ± 0.05	0.11 ± 0.04	0.65 ± 0.06
200	0.58 ± 0.02	0.08 ± 0.01	0.88 ± 0.07
400	0.71 ± 0.01	0.10 ± 0.01	1.91 ± 0.07
600	0.57 ± 0.05	0.14 ± 0.04	2.30 ± 0.10

is increased to 600 rpm the length of the nanoplates decreases since they get stacked.

Table 1 also shows that when rotation speed is increased, the width (w) of the nanostructures is enhanced from 0.08 μm at 200 rpm to 0.14 μm at 600 rpm. This is related to the interaction between the electrode surface and the complex soluble species in hydrodynamic conditions. Moreover, increasing the rotation speed of the electrode, the thickness of the nanostructured layer increases from 0.65 μm at 0 rpm to 2.30 μm at 600 rpm. Therefore, it can be elucidated that rotation speed during anodization of tungsten until 400 rpm might enhance the specific surface area of the nanoplates. However, if rotation speed is increased over 400 rpm small packed clusters are obtained over a heterogeneous WO_3 nanostructure, thus, hindering light harvesting (Figure 2A.4).

These tungsten oxide samples have been also studied by transmission electron microscopy (TEM) to gain additional information complementary to that provided by the FESEM study. Unlike the FESEM study, the TEM analysis was performed over the material collected through the scratching of the outer WOx layer. As mentioned before, the FESEM study showed similar morphology for all the samples although with significant differences in the width, length, and thickness of the nanoplates. Interestingly, the TEM analysis will provide additional notorious differences. According to the TEM images, the sample prepared in static conditions (0 rpm, Figure 2B.1) and that with an excessive rotation (600 rpm, Figure 2B.2) presented a compact aspect with scarce nanoporosity. Moreover, a rather flat surface was observed in both cases.

The optimal sample (400 rpm, Figure 2B.3,B.4) has been studied in detail, showing a more elongated shape than the others and a rougher surface. The most noteworthy aspect of this sample is the outer part, which is fully covered by small nanoparticles (most of them in the 5–10 nm range) strongly attached to the nanostructure. This way the active area of the surface of this nanostructure must be remarkably higher than that of the other samples.

To investigate the potential impact of hydrodynamic conditions on the crystallinity of WO_3 nanostructures, XRD examination was performed. The XRD patterns for the samples anodized at 0, 200, 400, and 600 rpm are shown in Figure 2C.

$$W + 3H_2O \rightarrow WO_3 + 6H^+ + 6e^- \quad (1)$$

$$WO_3 + 2H^+ \rightarrow WO_2^{2+} + H_2O \quad (2)$$

$$WO_3 + 6H^+ + nBF_4^- \rightarrow [W(BF_4)_n]^{(6-n)} + 3H_2O \quad (3)$$

$$WO_2^{2+} + 3H_2O \rightarrow WO_3 \cdot 2H_2O + 2H^+ \quad (4)$$

This graph shows that all samples display a pattern with peaks at ca. 2θ = 23°, 34°, 35°, 49°, and 58° characteristic of monoclinic WO_3 (JCPDS Card No. 43–1035). The (002), (020), and (200) planes of the monoclinic WO_3 are associated to the triplet that constitutes the major peak at 2θ = 23.15°, 23.48°, and 24.25°.[41] The presence of diffractions of metallic tungsten cannot be appreciated.[48] In order to compare the crystallite size (D) of the different samples Scherrer's equation has been used (Equation 5).[49]

$$D = \frac{\mathcal{K} \cdot \lambda}{\mathrm{FWHM} \cdot \cos(\theta)} \quad (5)$$

where the shape factor $\mathcal{K}$ is 0.9, the X-ray wavelength λ is 0.15406 nm, the full-width at half maximum (FWHM) intensity is obtained from each peak (in rad), and θ (rad) is the Bragg angle.[49] Crystallite sizes of WO_3 nanostructures anodized at 0, 200, 400, and 600 rpm are shown an on inset in (Figure 2C).

The results show that the size of the crystallite decreases when rotation speed is used during anodization. This fact could benefit the sample with the smallest crystal size (400 rpm), since a smaller crystal size can increase the photoelectrochemical behavior of the samples by improving the surface area and leading to better separation of charge carriers.[50,51] However, when increasing excessively the agitation up to 600 rpm, the crystal size slightly increases again.

Figure S1 shows, for comparison, the XRD study comparing the effect of calcination in the crystallinity for a WO_3 nanostructure anodized at 400 rpm. It is noticeable that the two XRD patterns are very similar, except for minor variations in the intensities of some peaks associated with the lower crystallinity of the uncalcined samples. This increased crystallinity is related to better conductivity and improved charge pairs generation.

Figure 2D shows the DR-UV–vis spectra of WO_3 samples anodized at different hydrodynamic conditions. For all samples, the optical absorption increases sharply around 450 nm, which is consistent with monoclinic WO_3.[52,53] The absorbance in the UV range (200–400 nm) is higher when the rotation speed increases until 600 rpm, displaying the nanostructure synthesized under static conditions the lowest intensity in this range.

The nanostructure anodized at 400 rpm presents the higher absorption in the UV range. However, in the visible range it can be observed that the 0 rpm sample shows better absorption, which could be beneficial in the photoelectrochemical applications with sunlight. Despite that, the more heterogeneous surface distribution of the nanoplates in the 0 rpm anodized WO_3 can lead to some recombination of the electron-hole pairs generated.

For a better understanding of the possible interaction of the samples with light radiation, the direct bandgap of WO_3 was calculated from the Tauc equation (Equation 6) by extrapolating the

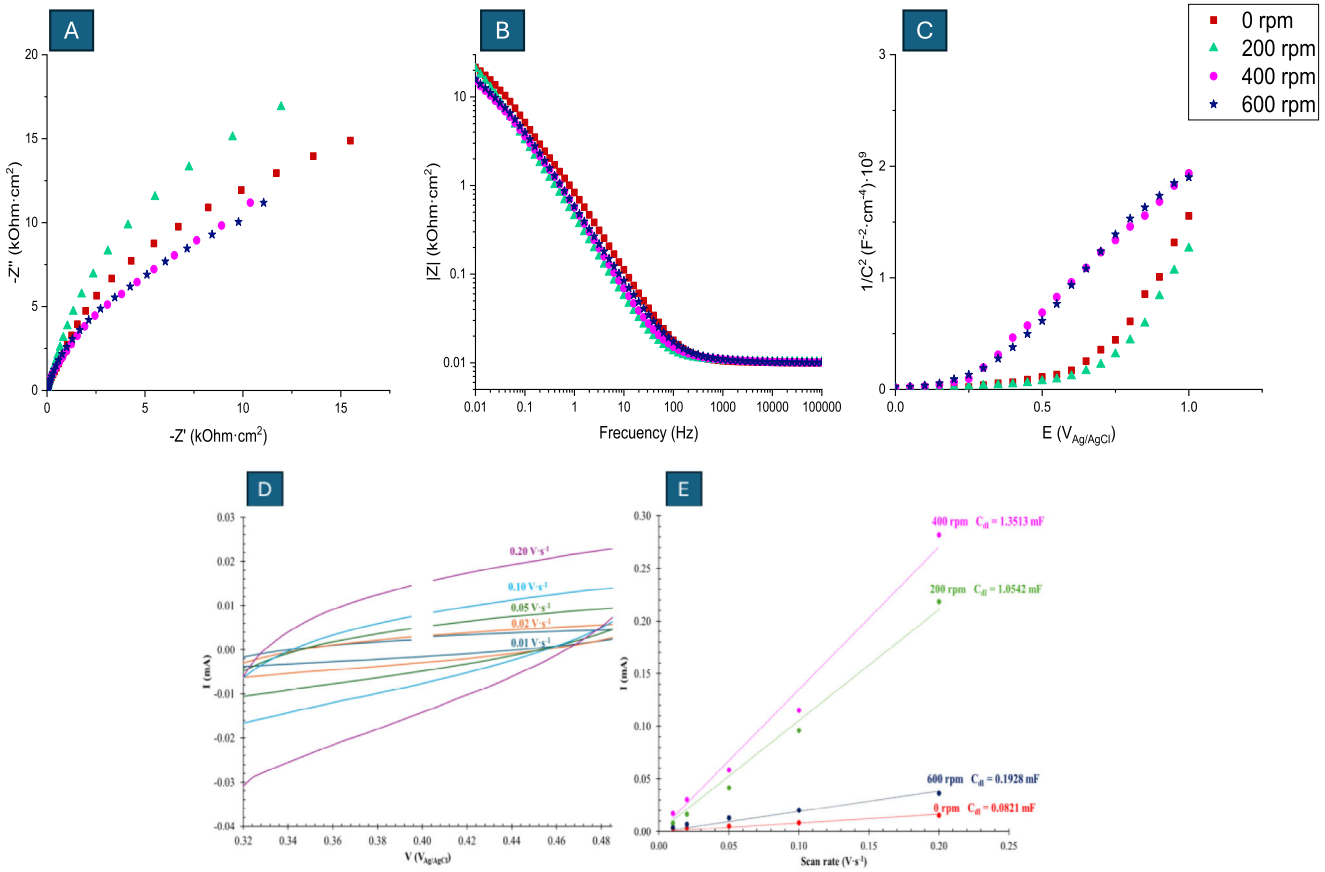

Figure 3. EIS data for the WO_3 nanostructures synthesized at different hydrodynamic conditions (0, 200, 400, and 600 rpm). (A) Nyquist, (B) Bode-module, (C) Mott–Schottky plots, (D) Representative (at 0 rpm) cyclic voltammetry of the WO_3 catalysts measured in a non-Faradaic region at different scan rates (0.01, 0.02, 0.05, 0.10, and 0.20 V s^{-1}) and (E) Anodic charging currents of the catalysts synthesized at different rpm measured at OCP as a function of scan rate.

linear section close to the onset versus "hν" (Figure S2).[53,54]

$$(Ah\nu)^n = K\left(h\nu - E_g\right) \quad (6)$$

According to the Tauc equation, "A" is the absorbance, "hν" is the photon energy, n is 0.5 for the indirect transition,[53] "E_g" is the bandgap energy, and "K" depends on the material. The calculated bandgaps are shown in Figure 2D. The bandgap for the nanostructure anodized under static conditions is similar to the values presented in literature as typical for WO_3.[31] Additionally, the bandgap values calculated for the WO_3 samples synthetized rotating the electrode during anodization decrease.

It is clear that the bandgap decreases with increasing agitation, although the values are similar ranging from 2.12 to 2.50 eV. Therefore, the use of controlled hydrodynamic conditions during anodization allows modifying the bandgap into a narrower one (2.12–2.20 eV) and allowing better mobility of the photogenerated charge carriers.[55]

Electrochemical processes at the nanostructure/electrolyte interface were examined using electrochemical impedance spectroscopy (EIS) measurements. The Nyquist and Bode plots are shown in Figure 3. Figure 3A shows two incomplete semicircles, one at medium frequencies and one at low frequencies. The second semicircle, which is considerably larger, explains the electrical behavior of the remaining compact oxide layer below the nanostructure. On the other hand, the first semicircle, which is smaller, can be associated with the interfacial charge transfer of the nanostructures.[41] Hence, it is evident that the two anodized samples at 400 and 600 rpm have the lowest second semicircle, while the samples at 0 and 200 rpm show a higher semicircle, which is associated with a higher charge transfer resistance.

Bode-module plot represented in Figure 3B is used to determine the resistance of the electrolyte (R_S) at the maximum frequency value and the total resistance of the nanostructure from the minimum frequency value (R_T). Consequently, in order to quantitively discuss EIS results, the values of the resistances have been determined (Table S1). Since the electrolyte and the experimental set up were constant, R_S values are very similar for all the samples. Comparing the different values of total charge resistance (R_T), a decrease with increasing agitation speed can be observed. Therefore, nanostructures formed under hydrodynamic conditions possess higher electrical conductivity, which leads to better photoelectrochemical performance. This fact may be related to agitation by improving the diffusion of ions along the electrolyte onto the surface of the tungsten substrate during anodization. However, the nanostructure anodized rotating the electrode at 600 rpm exhibits higher total resistance than the one synthesized at 400 rpm. This is likely due to the het-

Table 2. Donor densities values obtained for the WO_3 nanostructures anodized at different rpm.

WO_3 Sample (rpm)	N_D (cm^{-3})
0	$8.06 \cdot 10^{20}$
200	$8.19 \cdot 10^{20}$
400	$1.14 \cdot 10^{21}$
600	$1.01 \cdot 10^{21}$

erogeneous structure of the 600 rpm nanostructure (Figure 2A.4) caused by an excessive rotation speed, which lowers electron mobility.[56]

Mott–Schottky analysis was also performed to study the semiconducting behavior of the WO_3 nanostructures. Thus, Figure 3C shows the Mott–Schottky plots of the different nanostructures observing clearly a linear region with positive slope for all the samples, indicating an n-type semiconductivity.[37] Furthermore, from the different slopes using the Mot–Schottky equation (Equation 7) the donor density (N_D) values of the WO_3 nanostructures can be calculated, which are mainly oxygen vacancies in tungsten oxide.[37,57]

$$\frac{1}{C^2} = \frac{1}{C_H^2} + \frac{2}{\varepsilon_r \varepsilon_0 e N_D} \cdot \left(E - E_{FB} - \frac{k_B T}{e} \right) \quad (7)$$

where C_H is the capacitance of the Helmholtz layer, e is the elementary charge ($1.60 \cdot 10^{-19}$ C), E_{FB} (V) is the flat-band potential, k_B is the Boltzmann constant ($1.38 \cdot 10^{-23}$ J K^{-1}), T (K) is the absolute temperature, ε_r is the relative permitivity of dielectric constant of WO_3 (50), and ε_0 is the vacuum permittivity ($8.85 \cdot 10^{-14}$ F cm^{-1}).[37,58]

Thus, donor densities (N_D) of the different WO_3 nanostructures anodized at 0, 200, 400, and 600 rpm are shown in Table 2.

Table 2 shows that the introduction of agitation during anodization increases the concentration of oxygen vacancies. The anodized sample at 400 rpm presents the highest N_D value as a result of its homogeneous morphology (Figure 2A.3) with high specific surface area favoring electron transfer processes. In addition, the values of donor densities (N_D) obtained are consistent with the total charge-transfer resistances in Table S1 (R_T), since a higher oxygen vacancy density leads to greater electron mobility within the nanostructure and therefore, to higher conductivity (lower resistance).[59] This way, this enhancement in N_D values leads to an improvement in the activity of the catalysts.

Figure 3D shows representative cyclic voltammograms of the WO_3 catalyst anodized at 0 rpm measured in a non-Faradic region at different scan rates. At these conditions, the determined currents are assumed to be due to capacitive charging. Figure 3E presents the determined double-layer capacitance (C_{dl}) of the catalysts taken as the average of the absolute value of the slope (anodic and cathodic). Double layer capacitance values were taken as a qualitative estimation of the electrochemically active surface area (ECSA) of the samples (Equation 8) [60]:

$$ECSA = \frac{C_{DL}}{C_S} \quad (8)$$

where C_s is the specific capacitance of the sample.

After analyzing the results from all the synthesized catalysts (Figure 3E), it can be concluded that the sample synthesized at 400 rpm shows the highest double-layer capacitance value and the largest electrochemical surface area (ECSA). The catalyst anodized at 200 rpm exhibits the second highest C_{dl}, followed by the electrode synthesized at 600 rpm. The sample anodized under static conditions shows the lowest C_{dl} value.

According to the detailed characterization undertaken, the catalyst synthesized at 400 rpm presents the highest number of electrochemically active sites and, as a result, is the most promising for photoelectrochemical applications.

2.2. Photoelectrochemical Water Splitting

Photoelectrochemical H_2 production using WO_3 photoanodes under solar light irradiation was tested using light and dark pulses measuring their photocurrent densities in a 0.1 M H_2SO_4 solution. Figure 4A shows positive photocurrent densities (n-type semiconductor), the highest being achieved by the photoanode synthesized at 400 rpm (0.58 mA cm^{-2} at 1.00 V versus Ag/AgCl), while the sample anodized at 0 rpm showed a photocurrent density of 0.29 mA cm^{-2}. This better photoelectrochemical performance is in agreement with its better electrochemical and physicochemical characteristics.

Hydrogen production is interrelated with photocurrent density and Faraday's law can be used to calculate PEC H_2-gas production at 0.5 and 1.0 V versus Ag/AgCl. It is shown that a higher photocurrent density led to a higher production rate. Thus, the hydrogen production can be arranged in the sequence 400 > 200 > 600 > 0 rpm (Figure 4B). In accordance with the obtained results and the morphological and physical characteristics, different agitation speed during anodization affects the distribution of the nanoplates producing an increase in the photoelectroactivity of the catalyst. Furthermore, the nanostructure anodized at 400 rpm presents the lowest resistance, which allows a better mobility of the electron/hole pairs, reducing their recombination and increasing solar-to-hydrogen conversion efficiency, resulting in the generation of high amount of H_2. However, if rotation speed during anodization is increased to 600 rpm the photocurrent values are lower. This fact is associated with the more heterogeneous surface of this nanostructure (Figure 2A.4) and its higher crystallite size.

Table 3 compares the performance in the water splitting reaction of different WO_3 nanostructures reported in the literature with the best one synthesized in the present work (400 rpm). By analyzing the obtained photocurrent density, which is correlated with the hydrogen generated, it can be concluded that our nanoplates obtained by anodization (400 rpm sample) have better performance during water splitting than other WO_3-based nanocomposites. Actually, our nanostructure presents the highest thickness and nanoplate length (Table 3), therefore a higher surface/area is achieved. This fact is very important, as our fabrication method is very simple, requires mild conditions and does not use hazardous chemicals. It must be also noted that our

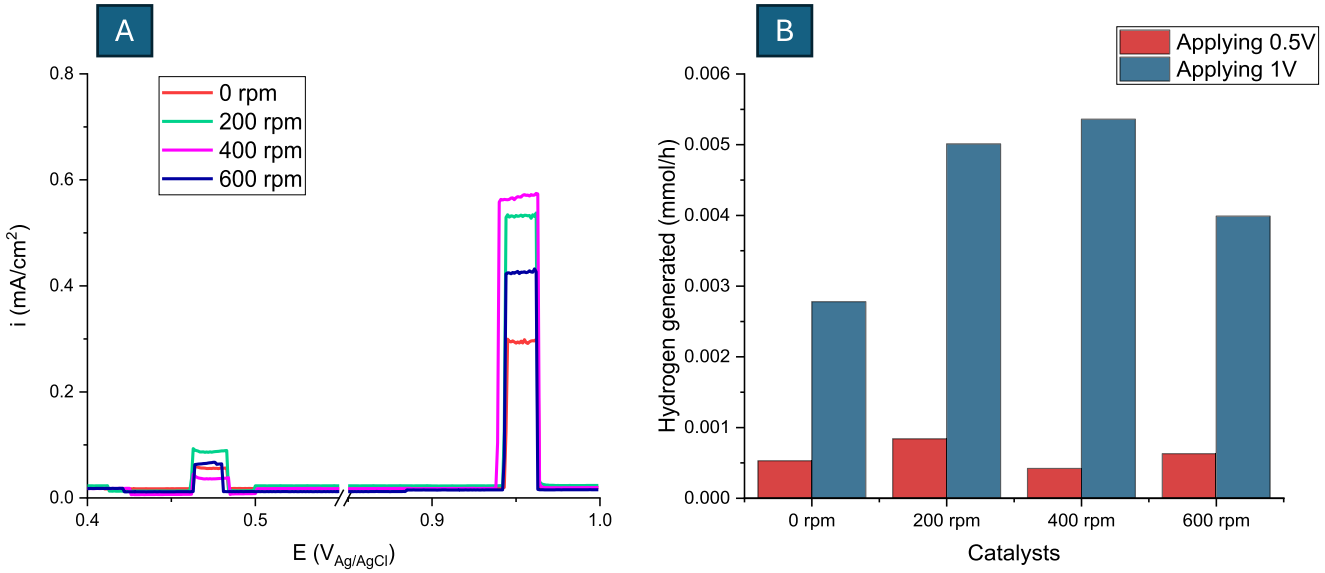

Figure 4. (A) Photocurrent density curves using a solar simulator irradiating the different WO_3 nanostructures anodized at 0, 200, 400, and 600 rpm and (B) Generated hydrogen by photoelectrochemical water splitting using the different WO_3 nanostructures.

Table 3. Water splitting efficiency of various WO_3 catalysts used in the literature.

Photoanode	Morphology	Nanostructure Dimensions	Light Source	Pec-ws Efficiency	Ref.
WO_3 NH_4OH treatment	Nanoporous	Thickness: 1220 nm Pore size: ~146 nm	300 W Xe lamp (AM 1.5G solar light)	0.45 mA/cm^2 at 1.00 $V_{Ag/AgCl}$	[62]
WO_3 deposited by sputtering	Sub-micrometric columnar structures	Thickness: - Size: ~ 94 × 62 nm	450 W Xe lamp (AM 1.5G solar light)	0.05 mA/cm^2 at 1.23 $V_{Ag/AgCl}$	[63]
WO_3 hydrothermal synthesis	Nanofiber	Thickness: 500 nm Pore size: 600 nm	300 W Xe lamp (AM 1.5G solar light)	0.10 mA/cm^2 at 1.23 V_{RHE}	[64]
Anodized WO_3	Nanocoral	Thickness: 610 nm Length: 550–600 nm	300 W Xe lamp (AM 1.5G solar light)	0.09 mA/cm^2 at 1.23 V_{RHE}	[65]
WO_3 sol–gel method	Nanoporous	Thickness: - Pore size: 500 nm	300 W Xe lamp (AM 1.5G solar light)	0.97 mA/cm^2 at 1.23 V_{RHE}	[66]
WO_3 Hydrothermal synthesis	Nanoplates	Thickness: - Size: ~ 194 × 135 nm	300 W Xe lamp (AM 1.5G solar light)	~0.30 mA/cm^2 at 1.23 V_{RHE}	[66]
Anodized WO_3	Nanoplates	Thickness: 1910 nm Size: 710 × 100 nm	300 W Xe lamp (AM 1.5G solar light)	0.58 mA/cm^2 at 1.00 $V_{Ag/AgCl}$	This work

nanostructure is composed solely of WO_3, without any type of promoter or co-catalyst such as other metallic nanoparticles or noble metals. A next step in the optimization of water splitting catalysts could be the selection of other metals to be deposited on this optimized WO_3 nanostructure as a basis.

2.3. Photoelectrochemical CO_2 Reduction

To transform carbon dioxide into valuable products through a photoelectrochemical approach, two of the WO_3 nanostructures synthesized have been used as photoanodes, which have been irradiated with solar light. After the careful electrochemical study carried out, the WO_3 nanostructure anodized at 400 rpm was selected since it presented the best morphological and electrochemical characteristics. Additionally, for comparative purposes, the WO_3 anodized without agitation was also tested. The cathode employed in all cases has been simple Cu.

The experiments undertaken led to the formation of different products such as formic acid, acetic acid, and methanol as a minority. Figure 5A shows the evolution of formic acid (black), methanol (red), and acetic acid (blue) concentration with the reaction time using the catalyst prepared at 400 rpm. At the beginning of the reaction, the concentration of the reaction products slowly increased. This fact corresponds mainly to the activation of CO_2, a step that is considered the limiting of the reaction.[14,61] After this period of approximately 1–2 h, an increase is observed in the formic acid concentration reaching the maximum at 6 h (~190 µmol/L). It seems that methanol formation competes with acetic acid production during the reac-

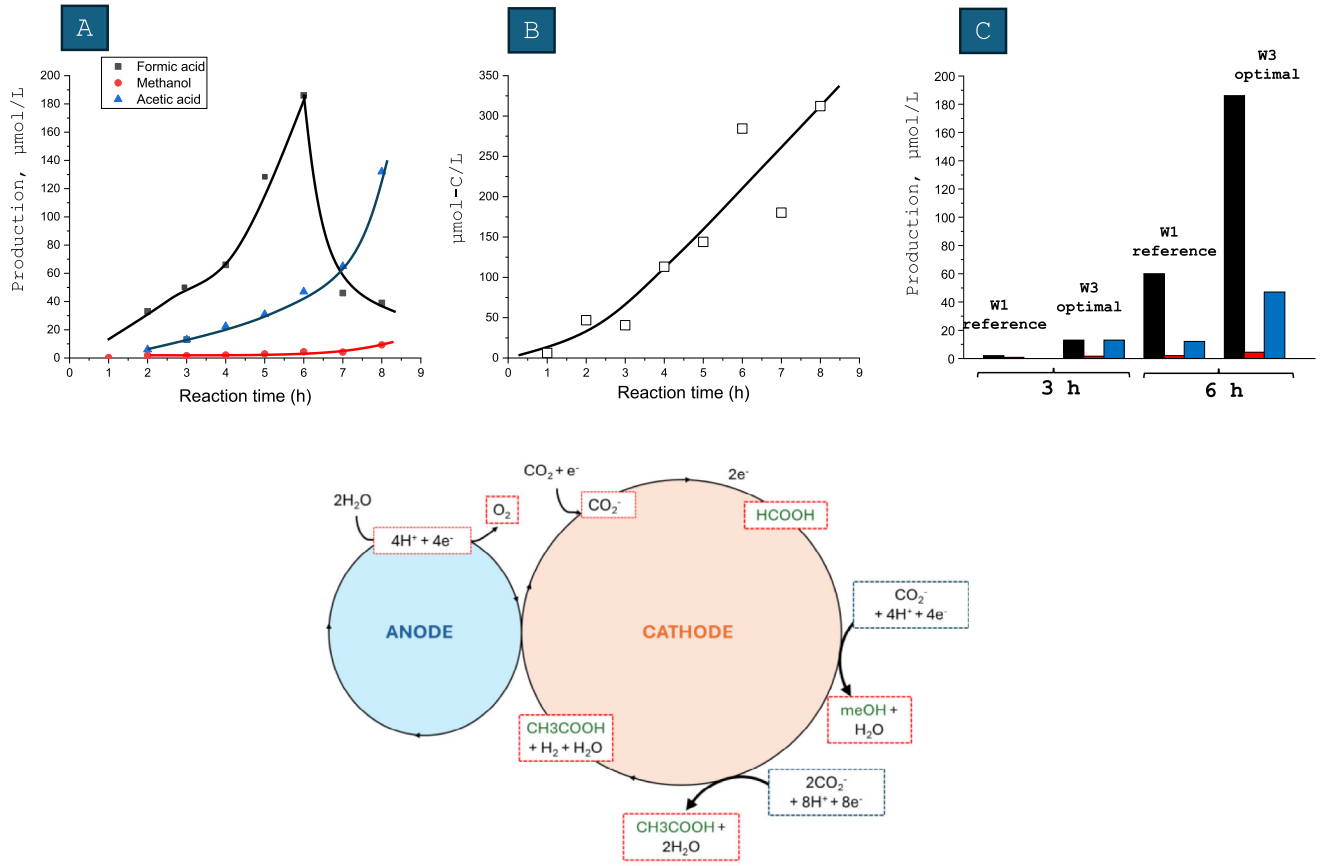

Figure 5. (A) Catalytic performance of nanostructured WO_3 in the CO_2 electroreduction. (A) Evolution of the production of formic acid (▪), methanol (•), and acetic acid (Δ) with the reaction time for the 400 rpm sample. (B) Evolution of the moles of C-products detected with the reaction time for the 400 rpm sample, (C) Production of formic acid (black), methanol (red), and acetic acid (blue) for the reference W1 (0 rpm) and the optimal W3 (400 rpm) samples after 3 and 6 h of reaction. Notes: Reaction conditions shown in text. (D) The lower part of the figure shows the possible photoelectrochemical CO_2 reduction pathways to obtain acetic acid, methanol, and formic acid.

tion. Importantly, we obtain a significant concentration of acetic acid after 8 h of experiment. We must mention that the system was left for 8 h without applying any type of external force, observing that there was no conversion to any of the products. This indicates, as well, that the cationic membrane was an excellent barrier separating anodic and cationic electrolytes. Figure 5B shows that the overall concentration of C-containing compounds detected in solution increases with the reaction time. This increase is accompanied by the acidification of the solution from 6.57 (time = 0 h) to 2.01 (time = 8 h), favored by the formation of acidic compounds. On the other hand, Figure 5C compares the performance of the optimized 400 rpm sample with that prepared without agitation. Interestingly, a remarkably higher production of C-compounds has been observed in the case of the sample prepared in dynamic conditions. Therefore, the use of optimized WO_3 nanostructures as photoanodes can be a highly interesting option, since it can absorb light more efficiently, increasing the photogenerated charges (e^-) in the surface.[56] Hence, the electrons in the CB are transferred to the cathode, increasing the availability of electrons to reduce CO_2 to acetic acid. Moreover, favoring the water oxidation reaction allows increasing the amount of available protons necessary for the transformation of CO_2.

In accordance with the obtained results, a possible simplified reaction pathway to obtain formic and acetic acid that has occurred during CO_2 electrochemical reduction in an acid medium is illustrated in Figure 5D. It is important to mention that, although the HER reaction (H_2O/H_2) is always present,[7,14] CO_2 reduction is the main reaction in the present study. Moreover, we have seen that the mechanism involves the formation of methanol as well.

After the accumulation of sufficient protons and electrons, the CO_2 electrochemical reduction begins with the absorption of the molecule and the subsequent activation in the catalyst surface by transferring an electron, forming the CO_2^- intermediate.[14,61,67] Then, when CO_2 is adsorbed and activated, the formate intermediate is produced in acid pH[68,69] (Equation 9).

$$CO_2^- + H^+ + e^- \rightarrow HCOO^- \quad (9)$$

Due to the high stability of CO_2, the anode reaction (OER) is very important since it provides a large number of protons and electrons that can facilitate this first step (Figure 5D). Moreover, when CO_2 is introduced into the solution, it is dissociated,

producing protons (Equation 10).

$$CO_2 \rightarrow H^+ + HCO_3^- \quad (10)$$

Then, a sequence of reactions involving H^+ occurs. First, the formate produced from the activation of CO_2 is hydrogenated, thus generating formic acid, as shown in Equation (11).[69,70]

$$HCOO^- + H^+ \rightarrow HCOOH\ (aq.) \quad (11)$$

Thereafter, formic acid could be reduced to methanol with the interaction of $4e^-$ and $4H^+$ (Equation 12).[68] This step is less common, and it needs the presence of a high concentration of protons in the solution.

$$HCOOH + 4H^+ + 4e^- \rightarrow CH_3OH + H_2O \quad (12)$$

During this process, the formation of acetic acid might also occur more slowly due to the interaction of more radical species (·), as explained below. Owing to the capability of copper to adsorb carbon species, the C—O bond can be stabilized, and it could be broken, forming a ·CHO intermediate.[29] This can undergo further reduction to $\cdot CH_2OH$, which may either desorb to form methanol or continue the reduction on the copper surface.[71] This process is shown below (Equations 13–15):

$$\cdot CHO + H^+ + e^- \rightarrow \cdot CH_2O \quad (13)$$

$$\cdot CH_2O + H^+ + e^- \rightarrow \cdot CH_2OH \quad (14)$$

$$\cdot CH_2OH + H^+ + e^- \rightarrow CH_3OH\ (aq.) \quad (15)$$

Whether the reduction process continues, the second C—O bond of the $\cdot CH_2OH$ radical can be broken into $\cdot CH_3$. Then, due to the presence of a large CO_2 concentration, formed methyl species are susceptible to nucleophilic attack by unadsorbed CO_2^-, leading to the formation of acetic acid.[29,72]

Moreover, we observe a decrease in the concentration of formic acid as opposed to the increase in acetic acid. Therefore, formic acid could interact as an intermediate, forming unstable $\cdot OCH_2OH$ species by its protonation (Equations 16 and 17),[71] and it might be reduced, obtaining H_2 as a subproduct.

$$\cdot HCOOH + H^+ + e^- \rightarrow \cdot OCH_2OH \quad (16)$$

$$\cdot OCH_2OH + H^+ + e^- \rightarrow H_2 + \cdot OCH_2O \quad (17)$$

Thereafter, OCH_2O^- may be reduced, forming water, as shown in Equation 18:[73]

$$OCH_2CO^- + H^+ \rightarrow H_2O + \cdot CH_2 \quad (18)$$

Finally, $\cdot CH_2$ interacts with the CO_2^- adsorbed on the surface, giving $\cdot CO\text{-}\cdot CH_2$[72,73] and that intermediate is responsible for the production of acetic acid.

3. Conclusion

In conclusion, highly photoelectrochemically active tungsten oxide nanoplates (WO_3) can be synthesized in mild conditions by electrochemical anodization with ILs [EMIM][BF4] and using hydrodynamic conditions. Moreover, the rotation speed during the preparation must be controlled to achieve the optimal performance and maximize the specific area, the sample prepared at 400 rpm presenting the best behavior. The 400 rpm sample shows a more elongated shape than the others and a rougher surface, leading to a remarkable active area. This fact is very important since a higher active area means more charge pairs, and it successfully prevents the recombination of photogenerated charge carriers. The optimized tungsten oxide sample presents promising results for both i) the evolution of hydrogen and ii) the activation/reduction of the CO_2 molecule, mainly yielding formic acid, methanol, and acetic acid. The optimal sample (400 rpm) presents better morphological and photoelectrochemical characteristics than the sample anodized at 0 rpm, producing more hydrogen in the water splitting process and more C-containing compounds in the CO_2 reduction.

4. Experimental Section

4.1. Synthesis of Nanostructures

The anodization technique was used for the formation of nanostructures on the metal surface. Tungsten (99.95%, 0.125 mm thick) sheets were cut in a circular shape of 1.3 cm^2 and then ultrasonically washed with acetone, ethanol, and deionized water for 2 min. An electrolyte of 1.5 M methanesulfonic, 95% (v/v) water, and 5% (v/v) [EMIM][BF4] was used. During anodization, 20 V were applied between tungsten (anode) and platinum (cathode), submerging both in the electrolyte for 4 h at 50 °C. These conditions have been selected based on previous work.[47] The hydrodynamic conditions were modified between 0, 200, 400, and 600 rpm. As far as we know, this is the first time that anodization of tungsten in this type of electrolyte is carried out rotating the electrode during the synthesis. After anodization, the samples were washed in deionized water and then calcined at 600 °C for 4 h in air in order to obtain ordered crystalline structures.

4.2. Morphological and Physical Characterization

The study of the structural, morphological, and crystalline structure of the oxides obtained was performed using different techniques. Field emission scanning electron microscopy (FE-SEM) operating at 5 kV and transmission electron microscopy (TEM) utilizing a high-contrast transmission electron microscope JEOL jem 1010 have been used to examine the morphology of the anodized tungsten. The samples were sonicated in pure ethanol for 5 min before the microscopy analysis. A drop of the resultant suspension was then put on a holey carbon film supported by a copper grid and left to dry. For the analysis of the crystallinity and phase identification, X-ray diffraction (XRD) has been used with a Philips X'Pert diffractometer equipped with a graphite monochromator operating at 40 kV and 30 mA and employing nickel-filtered Cu Kα radiation ($\lambda = 0.1542$ nm). Moreover, the study of photoresponse of the samples and their bandgap was calculated using a UV visible spec-

trophotometer (Shimadzu) operating in the 200–800 nm wavelength range.

4.3. Electrochemical Characterization

Electrochemical characterization was conducted in a three-electrode cell with the anodized tungsten film as the anode, platinum as the cathode, and Ag/AgCl (3 M KCl) as the reference electrode, and an electrolyte of 0.1 M H_2SO_4 solution was employed for all the essays.

To analyze the electrochemical properties of samples, electrochemical impedance spectroscopy (EIS) tests were performed at 1 $V_{Ag/AgCl}$ scanning frequencies from 100 kHz to 0.01 Hz. In addition, the specific capacitance (C_{dl}) of the catalysts anodized at the different rotation speeds was measured. The procedure involved performing cyclic voltammetry within a potential range that excludes faradaic processes, ensuring that only capacitive charging was measured. The potential was cycled from OCP $\pm$ 0.1 V (based on tests carried out in a wide range of potentials from the OCP as shown in Figure S3) for three cycles at scan rates of 0.01, 0.02, 0.05, 0.10, and 0.20 V s^{-1}. Moreover, to determine the semiconductor character of the samples and to calculate the number of charge carriers, Mott–Schottky (MS) plots were obtained at a frequency of 5000 Hz, scanning the potential from 0.0 to 1.0 $V_{Ag/AgCl}$ (WO_3).

4.4. Photoelectrochemical H_2 Production and CO_2 Production

The photoelectrochemical analysis was carried out using a solar simulator equipped with a 300 W Xe lamp and an AM 1.5G filter.

The evaluation of the hydrogen production from the water splitting using the WO_3 nanostructures was carried out with the same configuration three-electrode cell and an electrolyte of 0.1 M H_2SO_4 solution. Thus, the samples were subjected to light/dark conditions (16 s light, 4 s dark), applying a potential from 0 to 1.0 $V_{Ag/AgCl}$ at 100 mW cm^{-2}.

For the photoelectroreduction of carbon dioxide, an H-type cell[74] with two compartments separated by a cationic membrane (thickness of 0.180 mm Nafion N-117 membrane) was used (Figure 1B). One compartment was composed of a cathode (copper) and the Ag/AgCl reference electrode of 3 M KCl, and the other compartment contained the WO_3 nanostructured sample working as the photoanode. In the cathode compartment, for the purpose of promoting the chemical stability of the acid species formed during the reaction (formic and acetic acid), a solution of 0.1 M Na_2SO_4 (pH = 6.58) was used.[29] On the other hand, a solution of 0.1 M H_2SO_4 was used for the anode to assure the stability of WO_3.[47]

The reaction was carried out in continuous mode in order to treat larger volumes of CO_2 and try to improve its scalability.[75] During the reaction, the solution of the cathodic compartment was saturated with N_2 for 15 min at a flow rate of 20 mL/min. After this purge, CO_2 was fed for 30 min (20 mL/min), saturating the electrolyte completely, and thereafter, it was fed at a flow rate of 10 mL/min for the entire duration of the experiment (8 h). In addition, to study the advantage of using photoelectrocalytic technique by illuminating the photoanode, different experiments were carried out with the different nanostructures synthesized. The photoelectrocatalytic approach was carried out at a potential of 1 $V_{Ag/AgCl}$ and irradiating with the solar simulator at a distance of 10 cm.

Carboxylic acid products of PEC CO_2 were analyzed employing an ion chromatograph (Metrohm 883 Basica IC Plus Ionic Chromatograph) at room temperature using an eluent of 3.2 mM Na_2CO_3 + 1.0 mM $NaHCO_3$ aq. (column flow: 0.7 mL/min). Alcohol products were measured by gas chromatography (Shimadzu) using helium as a gas carrier (column flow: 1.04 mL/min).

Supporting Information

The authors have cited additional references within the Supporting Information.[30,31]

Acknowledgments

This research was funded by the Ministerio de Ciencia e Innovación-Agencia Estatal de Investigación through the projects PID2021-126235OB-C33 MCIN/AEI/10.13039/501100011033/FEDERUna manera de hacer Europa, UE P and TED2021-129555B–I00/AEI/10.13039/501100011033/Union Europea NextGenerationEU/PRTR and by the European Union NextGenerationEU/PRTR. A. Pérez-Calvo is also grateful to Ministerio de Ciencia, Innovación y Universidades (FPU23/02557), and G. Sánchez-García to the Generalitat Valenciana (CIACIF/2021/010).

Conflict of Interests

The authors declare no conflicts of interest.

Data Availability Statement

The data that support the findings of this study are available from the corresponding author upon reasonable request.

Keywords: Electrochemical anodization · Formic acid · Photoelectrochemical CO_2 reduction · Tungsten oxide nanoplates

[1] C. Wang, J. Song, D. Shi, J. L. Reyna, H. Horsey, S. Feron, Y. Zhou, Z. Ouyang, Y. Li, R. B. Jackson, *Nat. Commun.* **2023**, *14*, 6434.
[2] M. Filonchyk, M. P. Peterson, L. Zhang, V. Hurynovich, Y. He, *Sci. Total Environ.* **2024**, *935*, 173359.
[3] G. Dativo, E. La Greca, L. F. Liotta, V. La Parola, M. Condorelli, G. Impellizzeri, G. Compagnini, S. Sciré, R. Fiorenza, *J. CO2 Util.* **2024**, *82*, 102765.
[4] L. Zhao, H. Y. Hu, A. G. Wu, A. O. Terent'ev, L. N. He, H. R. Li, *J. CO2 Util.* **2024**, *82*, 102753.
[5] J. Yu, X. Hao, L. Mu, W. Shi, G. She, *Chem. – A European J.* **2024**, *30*, 1–22.
[6] K. Irikura, J. A. L. Perini, J. B. S. Flor, R. C. G. Frem, M. V. B. Zanoni, *J. CO2 Util.* **2021**, *43*, 101364.
[7] H. R. Zhu, H. M. Xu, C. J. Huang, Z. J. Zhang, Q. N. Zhan, T. Y. Shuai, G. R. Li, *Chin. J. Catal.* **2024**, *62*, 53–107.
[8] J. Wang, J. Xiong, H. Guo, Y. Wei, *ChemCatChem* **2024**, *16*, e202400707.
[9] X. Zhang, W. Yu, Y. Guo, S. Li, Y. Chen, H. Wang, Z. Bian, *Chem. Eng. J.* **2023**, *455*, 140801.
[10] M. Li, Q. Wang, Y. He, Y. Wang, K. Wang, P. Tsiakaras, S. Song, *Coord. Chem. Rev.* **2023**, *495*, 215373.
[11] S. Tao, S. Liu, L. Zhang, T. Li, B. Qiu, G. Li, F. Shi, X. Cui, *ChemCatChem* **2024**, e202401546.
[12] J. Li, J. Ren, S. Li, G. Li, M. M. J. Li, R. Li, Y. S. Kang, X. Zou, Y. Luo, B. Liu, Y. Zhao, *Green Energy Environ.* **2024**, *9*, 859–876.
[13] T. F. Qahtan, T. O. Owolabi, O. E. Olubi, A. Hezam, *Coord. Chem. Rev.* **2023**, *492*, 215276.
[14] X. Chang, T. Wang, J. Gong, *Energy Environ. Sci.* **2016**, *9*, 2177–2196.
[15] P. Chen, Y. Zhang, Y. Zhou, F. Dong, *Nano Mater. Sci.* **2021**, *3*, 344–367.
[16] H. Xu, Y. Shen, X. Guo, L. Zhang, *Mater. Today Chem.* **2023**, *34*, 101802.

[17] T. M. David, P. R. Dev, P. Wilson, P. Sagayaraj, T. Mathews, *Electrochem. Sci. Adv.* **2022**, *2*, 1–64.
[18] G. Sánchez-García, A. Pérez-Calvo, R. M. Fernández-Domene, E. Blasco-Tamarit, R. Sánchez-Tovar, B. Solsona, *Dalton Trans.* **2023**, *52*, 14453–14464.
[19] K. Kobayashi, S. N. Lou, Y. Takatsuji, T. Haruyama, Y. Shimizu, T. Ohno, *Electrochim. Acta* **2020**, *338*, 135805.
[20] Z. Yang, J. Yang, H. Yang, F. Gao, C. Nan, R. Chen, Y. Zhang, X. Gao, Y. Yuan, Y. Jia, Y. Yang, *ChemPlusChem* **2024**, *89*, e202400309.
[21] Y. Yang, F. Zhan, H. Li, W. Liu, S. Yu, *J. Solid State Electrochem.* **2017**, *21*, 2231–2240.
[22] H. Zhao, J. Kang, H. Nan, G. Yang, H. Wei, H. Chen, G. Wang, H. Lin, *ChemistrySelect* **2019**, *4*, 2892–2897.
[23] S. T. Guo, Z. Y. Tang, Y. W. Du, T. Liu, T. Ouyang, Z. Q. Liu, *Appl. Catal. B* **2023**, *321*, 122035.
[24] S. Sato, T. Arai, T. Morikawa, K. Uemura, T. M. Suzuki, H. Tanaka, T. Kajino, *J. Am. Chem. Soc.* **2011**, *133*, 15240–15243.
[25] B. Zhou, X. Kong, S. Vanka, S. Cheng, N. Pant, S. Chu, P. Ghamari, Y. Wang, G. Botton, H. Cuo, Z. Mi, *Energy Environ. Sci.* **2019**, *12*, 2842–2848.
[26] S. Ding, C. Zhu, H. Hojo, H. Einaga, *Appl. Catal. B* **2023**, *323*, 122099.
[27] W.-N. Wang, J. Soulis, Y. J. Yang, P. Biswas, *Aerosol Air Qual. Res.* **2014**, *14*, 533–549.
[28] A. Peugeot, C. E. Creissen, M. W. Schreiber, M. Fontecave, *ChemElectroChem* **2021**, *8*, 2726–2736.
[29] M. Orlić, C. Hochenauer, R. Nagpal, V. Subotić, *Energy Convers Manag.* **2024**, *314*, 118601.
[30] S. E. Jun, J. K. Lee, S. Ryu, H. W. Jang, *ChemCatChem* **2023**, *15*, e202300926.
[31] K. Hkiri, H. E. A. Mohamed, N. Harrisankar, A. Gibaud, E. van Steen, M. Maaza, *Catal. Commun.* **2024**, *187*, 106851.
[32] E. Boateng, S. S. Thind, S. Chen, A. Chen, *Electrochem. Sci. Adv.* **2022**, *2*, e2100146.
[33] Y. Li, L. Zhang, R. Liu, Z. Cao, X. Sun, X. Liu, J. Luo, *ChemCatChem* **2016**, *8*, 2765–2770.
[34] Y. Wang, L. Yao, L. Xu, W. Wu, W. Lin, C. Zheng, Y. Feng, X. Gao, *Mater. Lett.* **2021**, *302*, 130460.
[35] S. S. Kaplan, M. S. Sonmez, *Mater. Chem. Phys.* **2020**, *240*, 122152.
[36] M. V. Santhosh, K. S. Devaky, M. K. Jayaraj, *Mater. Today Proc.* **2020**, pp. 183–185.
[37] N. A. Arzaee, M. F. Mohamad Noh, A. Aadenan, I. N. Nawas Mumthas, F. F. Ab Hamid, N. N. Kamarudin, N. A. Mohamed, M. A. Ibrahim, A. F. Ismail, M. A. Mat Teridi, *Chem. Eng. Sci.* **2022**, *252*, 117294.
[38] S. Poongodi, P. S. Kumar, D. Mangalaraj, N. Ponpandian, P. Meena, Y. Masuda, C. Lee, *J. Alloys Compd.* **2017**, *719*, 71–81.
[39] Z. Wan, C. Ge, L. Bai, S. Hussain, G. Liu, G. Qiao, M. Wang, *Ceram. Int.* **2024**, *50*, 36900–36907.
[40] M. M. Abouelela, G. Kawamura, W. K. Tan, A. Matsuda, *J. Colloid Interface Sci.* **2023**, *629*, 958–970.
[41] E. Da Silva, G. Sánchez-García, A. Pérez-Calvo, R. M. Fernández-Domene, B. Solsona, R. Sánchez-Tovar, *Materials* **2024**, *17*, 1243.
[42] P. Sharma, S. Sharma, H. Kumar, *J. Mol. Liq.* **2024**, *393*, 123447.
[43] N. Najarbashi, M. Baghban Salehi, F. Saghandali, B. Mokhtarani, M. Mirzaei, A. Sharifi, *Fuel* **2024**, *377*, 132811.
[44] J. Łuczak, M. Paszkiewicz, A. Krukowska, A. Malankowska, A. Zaleska-Medynska, *Adv. Colloid Interface Sci.* **2016**, *230*, 13–28.
[45] A. Pancielejko, M. Kroczewska-Gnatowska, P. Mazierski, J. Łuczak, A. Zaleska-Medynska, *Chem. Eng. J.* **2024**, *498*, 155274.
[46] E. Lassner, W.-D. Schubert, *Tungsten*, Springer, US, Boston, MA, **1999**.
[47] R. M. Fernández-Domene, A. Cháfer-Ortega, J. A. Lombana-Fernández, R. Sánchez-Tovar, B. Solsona, *Ceram. Int.* **2023**, *49*, 15434–15441.
[48] C. H. Henager, W. Jiang, T. Jiang, K. Kruska, R. J. Kurtz, Fusion Materials Semiannual Progress Report for the Period Ending **2016**, *61*, 115–119.
[49] V. S. Vinila, J. Isac, in *Design, Fabrication, and Characterization of Multifunctional Nanomaterials*, Elsevier, Amsterdam, the Netherlands **2021**, pp. 319–341.
[50] H. Lin, C. P. Huang, W. Li, C. Ni, S. I. Shah, Y. H. Tseng, *Appl. Catal. B* **2006**, *68*, 1–11.
[51] D. Prieur, W. Bonani, K. Popa, O. Walter, K. W. Kriegsman, M. H. Engelhard, X. Guo, R. Eloirdi, T. Gouder, A. Beck, T. Vitova, A. C. Scheinost, K. Kvashnina, P. Martin, *Inorg. Chem.* **2020**, *59*, 5760–5767.
[52] P. M. Kodam, P. A. Ghadage, D. Y. Nadargi, K. P. Shinde, I. S. Mulla, J. S. Park, S. S. Suryavanshi, *Ceram. Int.* **2022**, *48*, 17923–17933.
[53] K. Baishya, J. S. Ray, P. Dutta, P. P. Das, S. K. Das, *Appl. Phys. A Mater. Sci. Process* **2018**, *124*, 704.
[54] M. Iqbal, A. A. Thebo, W. B. Jatoi, M. T. Tabassum, M. U. Rehman, K. H. Thebo, M. A. Mohsin, S. Ullah, A. H. Jatoi, I. Shah, *Inorg. Chem. Commun.* **2020**, *116*, 107902.
[55] M. Kang, J. Liang, F. Wang, X. Chen, Y. Lu, J. Zhang, *Mater. Res. Bull.* **2020**, *121*, 110614.
[56] P. Cheng, Y. Yang, *Acc. Chem. Res.* **2020**, *53*, 1218–1228.
[57] Y. Liu, Y. Li, W. Li, S. Han, C. Liu, *Appl. Surf. Sci.* **2012**, *258*, 5038–5045.
[58] F. Amano, M. Tian, B. Ohtani, A. Chen, *J. Solid State Electrochem.* **2012**, *16*, 1965–1973.
[59] Y. C. Liu, J. A. Koza, J. A. Switzer, *Electrochim. Acta* **2014**, *140*, 359–365.
[60] C. C. L. McCrory, S. Jung, J. C. Peters, T. F. Jaramillo, *J. Am. Chem. Soc.* **2013**, *135*, 16977–16987.
[61] A. Marcos-Madrazo, C. Casado-Coterillo, Á.n. Irabien, *ChemElectroChem* **2019**, *6*, 5273–5282.
[62] Y. W. Choi, S. Kim, M. Seong, H. Yoo, J. Choi, *Appl. Surf. Sci.* **2015**, *324*, 414–418.
[63] D. Valerini, S. Hernández, F. Di Benedetto, N. Russo, G. Saracco, A. Rizzo, *Mater. Sci. Semicond. Process.* **2016**, *42*, 150–154.
[64] S. Xu, D. Fu, K. Song, L. Wang, Z. Yang, W. Yang, H. Hou, *Chem. Eng. J.* **2018**, *349*, 368–375.
[65] E. Park, J. E. Yoo, K. Lee, *Sustain. Energy Fuels* **2024**, *8*, 1448–1456.
[66] G. Zheng, S. Jiang, F. Zhang, H. Yu, Y. L. Zhang, *Appl. Phys. A Mater. Sci. Process* **2025**, *131*, 175901.
[67] Q. Shen, Z. Chen, X. Huang, M. Liu, G. Zhao, *Environ. Sci. Technol.* **2015**, *49*, 5828–5835.
[68] M. H. Miles, A. N. Fletcher, G. E. Mcmanis, L. O. Spreer, *J. Electroanal. Chem.* **1985**, *190*, 157–170.
[69] K. Fernández-Caso, G. Díaz-Sainz, M. Alvarez-Guerra, A. Irabien, *ACS Energy Lett.* **2023**, *8*, 1992–2024.
[70] B. Xiong, Y. Yang, J. Liu, *J. Phys. Chem. C* **2023**, *127*, 196–204.
[71] T. Biswal, K. P. Shadangi, P. K. Sarangi, R. K. Srivastava, *Chemosphere* **2022**, *298*, 134299.
[72] H. Qi, X. Han, J. Fu, J. Ma, X. Jia, M. Zhao, X. Wang, Z. Fu, J. Zhang, X. Zhao, *J. Environ. Chem. Eng.* **2025**, *13*, 115058.
[73] X. Wang, C. Gao, J. Low, K. Mao, D. Duan, S. Chen, R. Ye, Y. Qiu, J. Ma, X. Zheng, R. Long, X. Wu, L. Song, J. Zhu, Y. Xiong, *Sci. Bull.* **2021**, *66*, 1296–1304.
[74] B. Liu, T. Wang, S. Wang, G. Zhang, D. Zhong, T. Yuan, H. Dong, B. Wu, J. Gong, *Nat. Commun.* **2022**, *13*, 7111.
[75] Y. Pan, H. Zhang, B. Zhang, F. Gong, J. Feng, H. Huang, S. Vanka, R. Fan, Q. Cao, M. Shen, Z. Li, Z. Zou, R. Xiao, S. Chu, *Nat. Commun.* **2023**, *14*, 1013.

Manuscript received: April 24, 2025
Revised manuscript received: June 6, 2025
Accepted manuscript online: June 8, 2025
Version of record online: June 28, 2025